nanomaterials

MDPI

Article

Dimension-Dependent Bandgap Narrowing and Metallization in Lead-Free Halide Perovskite $Cs_3Bi_2X_9$ (X = I, Br, and Cl) under High Pressure

Guangbiao Xiang [1], Yanwen Wu [1], Man Zhang [1], Chen Cheng [1,*], Jiancai Leng [2,*] and Hong Ma [1,*]

[1] Shandong Provincial Key Laboratory of Optics and Photonic Device, Collaborative Innovation Center of Light Manipulations and Applications, School of Physics and Electronics, Shandong Normal University, Jinan 250014, China; m17753643157@163.com (G.X.); yanwenwu1209@163.com (Y.W.); zhangman010501@163.com (M.Z.)

[2] School of Electronic and Information Engineering (Department of Physics), Qilu University of Technology (Shandong Academy of Sciences), Jinan 250353, China

* Correspondence: drccheng@sdnu.edu.cn (C.C.); jiancaileng@qlu.edu.cn (J.L.); mahong@sdnu.edu.cn (H.M.)

Abstract: Low-toxicity, air-stable cesium bismuth iodide $Cs_3Bi_2X_9$ (X = I, Br, and Cl) perovskites are gaining substantial attention owing to their excellent potential in photoelectric and photovoltaic applications. In this work, the lattice constants, band structures, density of states, and optical properties of the $Cs_3Bi_2X_9$ under high pressure perovskites are theoretically studied using the density functional theory. The calculated results show that the changes in the bandgap of the zero-dimensional $Cs_3Bi_2I_9$, one-dimensional $Cs_3Bi_2Cl_9$, and two-dimensional $Cs_3Bi_2Br_9$ perovskites are 3.05, 1.95, and 2.39 eV under a pressure change from 0 to 40 GPa, respectively. Furthermore, it was found that the optimal bandgaps of the Shockley–Queisser theory for the $Cs_3Bi_2I_9$, $Cs_3Bi_2Br_9$, and $Cs_3Bi_2Cl_9$ perovskites can be reached at 2–3, 21–26, and 25–29 GPa, respectively. The $Cs_3Bi_2I_9$ perovskite was found to transform from a semiconductor into a metal at a pressure of 17.3 GPa. The lattice constants, unit-cell volume, and bandgaps of the $Cs_3Bi_2X_9$ perovskites exhibit a strong dependence on dimension. Additionally, the $Cs_3Bi_2X_9$ perovskites have large absorption coefficients in the visible region, and their absorption coefficients undergo a redshift with increasing pressure. The theoretical calculation results obtained in this work strengthen the fundamental understanding of the structures and bandgaps of $Cs_3Bi_2X_9$ perovskites at high pressures, providing a theoretical support for the design of materials under high pressure.

Keywords: cesium bismuth iodide perovskite; first-principles study; high pressure; bandgap narrowing; metallization

Citation: Xiang, G.; Wu, Y.; Zhang, M.; Cheng, C.; Leng, J.; Ma, H. Dimension-Dependent Bandgap Narrowing and Metallization in Lead-Free Halide Perovskite $Cs_3Bi_2X_9$ (X = I, Br, and Cl) under High Pressure. *Nanomaterials* **2021**, *11*, 2712. https://doi.org/10.3390/nano11102712

Academic Editor: Wolfgang Heiss

Received: 26 September 2021
Accepted: 12 October 2021
Published: 14 October 2021

1. Introduction

Organic–inorganic hybrid perovskites have attracted much attention from the researcher community because of their remarkable photoelectric properties, including high absorption coefficients in the visible light region, tunable bandgaps, high quantum yields, high carrier mobilities, and low effective carrier quality [1–6]. In addition, their processing is economical and utilizes simple solution treatments [7,8]. The power conversion efficiency (PCE) of perovskite solar cells (PSCs) has increased dramatically from 3.8% in 2009 to 25.5% [9,10]. Lead hybrid perovskites have the outstanding photovoltaic properties and a high PCE. However, the high toxicity of lead is a major challenge for the large-scale fabrication and commercialization of lead-based PSCs. Recently, nontoxic, all-inorganic, lead-free Bi-based perovskites have attracted significant attention owing to their stability, high photoluminescence, high quantum yield, and tunable bandgaps [11–17]. They have been widely used in applications, such as memory devices, photodetectors, solar cells, and X-ray detectors [18–26]. However, many studies have shown that there are some challenges

to overcome for the use of $Cs_3Bi_2X_9$ (X = I, Br, and Cl) perovskites in photovoltaic devices. The large bandgap (>2 eV) is the most important factor causing a low PCE, which limits their absorption efficiency and carrier transport performance. According to the Shockley–Queisser theory, a semiconductor with a bandgap in the range of 1.3–1.5 eV is an ideal material for solar cells. Although the PCE of Bi-based PSCs has improved slightly with the improvement of the thin-film technology, it still lags far behind that of lead-based perovskites. The traditional chemical modification cannot overcome this inherent limit. Therefore, tuning the bandgap with the aim of improving the photovoltaic performance of the $Cs_3Bi_2X_9$ perovskites has become a key challenge.

High pressure (HP), which is a non-polluting tuning method, is widely used to modulate the physical and chemical properties of materials without changing their chemical composition [27,28]. In recent years, the properties of halide perovskites have been widely studied under HP; the properties studied include piezochromism, bandgap engineering, structural phase transitions and optical properties, [29–32]. In addition, various novel physical phenomena have been observed under HP conditions. For example, the organic–inorganic hybrid perovskite nanocrystals present the comminution and recrystallization under HP and exhibit higher photoluminescence quantum yield and a shorter carrier lifetime [29]. A reversible amorphization has been observed for the $CH_3NH_3PbBr_3$ perovskite under a pressure of approximately 2 GPa; during this transition, the resistance increased by five orders of magnitude, and the material still retained its response to the visible light and semiconductor characteristics up to a pressure of 25 GPa [33]. Notably, pressure-induced structural changes and optical properties are reversible upon decompression, and a semiconductor–metal transition can be observed at 28 GPa [34]. It is notable that there are few studies on $Cs_3Bi_2X_9$ perovskite systems of different dimensions at HP [34,35], and no reports exist on the one-dimensional halide perovskite $Cs_3Bi_2Cl_9$.

In this work, we calculated the lattice constants, band structures, density of states (DOS), and optical properties of the one-dimensional perovskite $Cs_3Bi_2Cl_9$ via the density functional theory (DFT) under HP for the first time and compared with the zero-dimensional perovskite $Cs_3Bi_2I_9$ and the two-dimensional perovskite $Cs_3Bi_2Br_9$. We discussed the relationship between the bandgap of the $Cs_3Bi_2X_9$ perovskites and the HP and focused on the optimal bandgap of the Shockley–Queisser theory of the $Cs_3Bi_2X_9$ perovskites. The $Cs_3Bi_2I_9$ perovskite completed the transition from semiconductor to metal at 17.3 GPa, this finding indicated that HP is an effective means to induce the semiconductor–metal transition. Moreover, it was found that the lattice constants and bandgaps of the $Cs_3Bi_2X_9$ perovskites are dependent upon dimension, that is, the changes in the lattice constants and bandgap gradually decrease as the dimension increases from zero to two under the same pressure. Our calculated results obtained in this work strengthen the basic understanding of different structures of the $Cs_3Bi_2X_9$ (X = I, Br and Cl), providing theoretical guidance for the structure and bandgap regulation of Bi-based perovskites under HP.

2. Computational Model and Method

The DFT was performed in the Vienna *Ab-initio* Simulation Package (VASP) using the projected augmented wave (PAW) framework [36,37]. DFT is derived from the Schrodinger equation under the Born–Oppenheimer approximation, described by the Hohenberg–Kokn theorem and the Kohn–Sham equation. The pseudopotential is a hypothetical potential energy function used in place of the inner electron wave function to reduce the computation. The electron exchange–correction function was obtained via the generalized gradient approximation (GGA) parameterized using the Perdew–Burke–Ernzerhof (PBE) formalism [38]. The cut-off energy of the plane wave was set to 500 eV [34]. The convergence criteria for the energy and force were set to 10^{-5} eV and 0.01 eV/Å, respectively. The Brillouin zone integration were sampled with $4 \times 4 \times 4$, $4 \times 4 \times 4$, and $4 \times 4 \times 2$ Gamma-pack k-point meshes during the structure optimization of $Cs_3Bi_2I_9$, $Cs_3Bi_2Br_9$, and $Cs_3Bi_2Cl_9$, respectively. The entire optimization of the structures was completely relaxed [39]. The

valence electronic configurations of the Cs, Bi, I, Br, and Cl atoms are $5s^2 5p^6 6s^1$, $5d^{10} 6s^2 6p^3$, $5s^2 5p^5$, $4s^2 4p^5$, and $3s^2 3p^5$, respectively. The Γ Brillouin zone center has a highly symmetric path, with coordinates Γ (0, 0, 0) to the M (0.5, 0, 0), K (0.333, 0.333, 0), Γ (0, 0, 0), A (0, 0, 0.5), L (0.5, 0, 0.5), and H (0.333, 0.333, 0.5). The spin–orbit coupling is not considered due to the high computational cost. Previous studies have shown that higher levels of calculation (including the spin–orbit coupling, the GW method, or hybrid functionals) obtain more accurate bandgaps; However, they induce little change in the band structure of the heavy-metal halide perovskites [40].

3. Results and Discussion

The structures of the three halogenated perovskite crystals $Cs_3Bi_2X_9$ (X = I, Br, and Cl) are shown in Figure 1. The one-dimensional $Cs_3Bi_2Cl_9$ perovskite has an orthogonal-crystal structure; the two-dimensional $Cs_3Bi_2Br_9$ perovskite and the zero-dimensional $Cs_3Bi_2I_9$ perovskite have hexagonal cells [41,42]. The numbers of atoms in the $Cs_3Bi_2I_9$, $Cs_3Bi_2Br_9$, and $Cs_3Bi_2Cl_9$ perovskites in the primitive cell are 28, 14, and 56, respectively. The Bi atom is located at the center of the octahedron in the $Cs_3Bi_2X_9$ perovskites and is surrounded by six halogen atoms. Unlike in lead-based perovskites, in the $Cs_3Bi_2Br_9$ and $Cs_3Bi_2Cl_9$ perovskites, two octahedrons share one X atom (X = Br or Cl), whereas two octahedrons share three X atoms in the $Cs_3Bi_2I_9$ perovskite. X atoms with different sizes and the Bi atoms form a novel double-perovskite structure. Figure 2 shows the changes in the lattice parameters and volume of the $Cs_3Bi_2X_9$ perovskites under HP. In the primary cell of the $Cs_3Bi_2I_9$ and $Cs_3Bi_2Br_9$ perovskites, the lattice constants a and b are equal. The lattice constant and volume of $Cs_3Bi_2X_9$ clearly decrease with an increase in pressure, and the slope also decreases gradually. As is well established, pressure induces a reduction in the lattice constant. From a microscopic point of view, the pressure shrinks the distance between two atoms. The strong Coulomb force makes it increasingly difficult to further compress the material as the pressure increases.

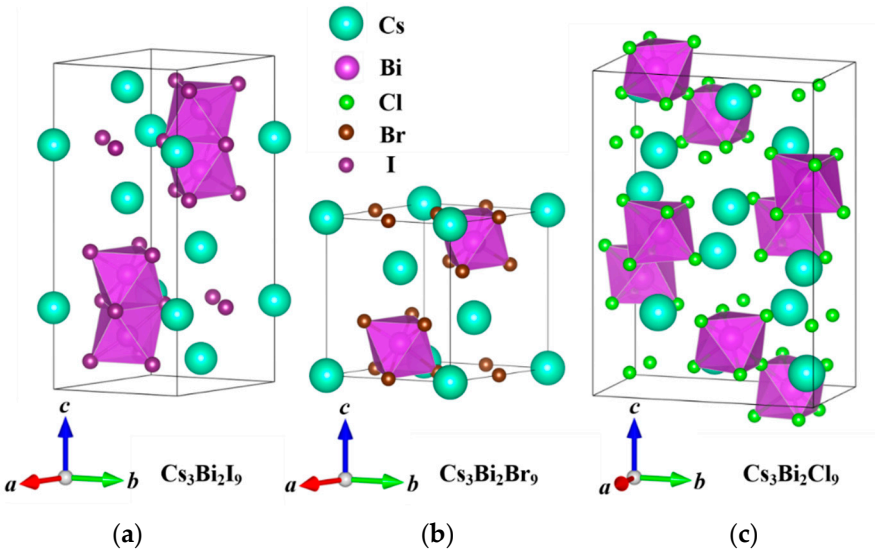

Figure 1. Crystal structures of the zero-dimensional perovskite $Cs_3Bi_2I_9$ (**a**), two-dimensional perovskite $Cs_3Bi_2Br_9$ (**b**), and one-dimensional perovskite $Cs_3Bi_2Cl_9$ (**c**).

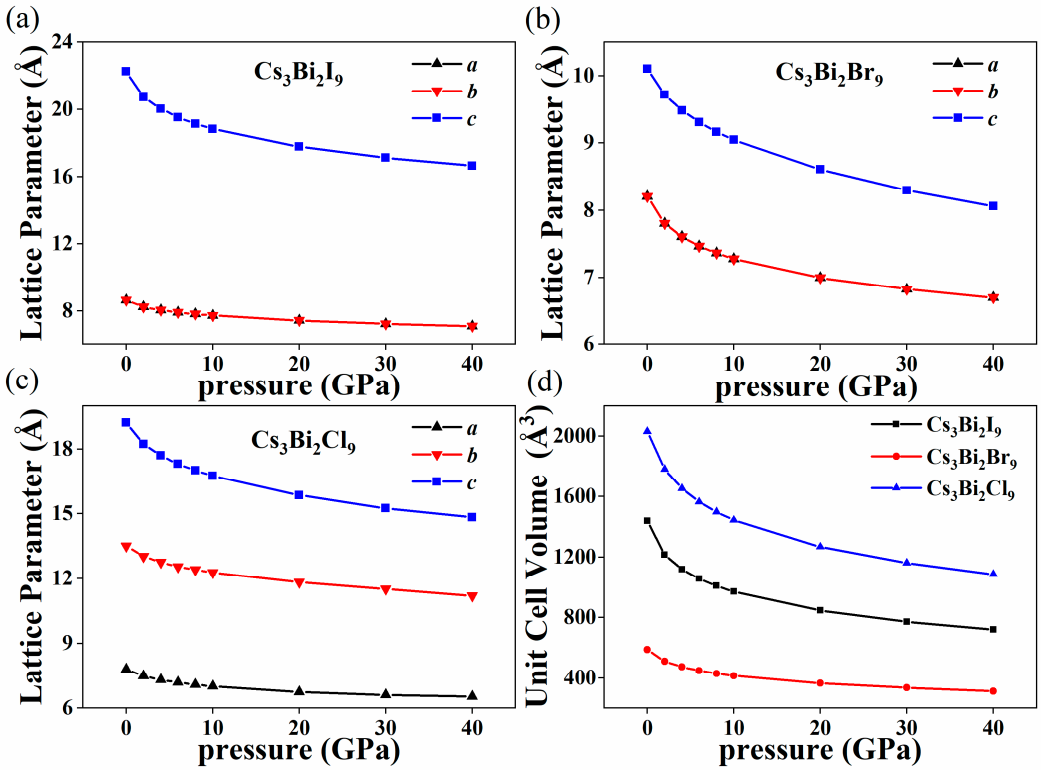

Figure 2. Changes in the calculated lattice parameter as a function of pressure from 0 GPa to 40 GPa for the $Cs_3Bi_2I_9$ perovskite (**a**), $Cs_3Bi_2Br_9$ perovskite (**b**), and $Cs_3Bi_2Cl_9$ perovskite (**c**). Changes in the unit cell volume of the $Cs_3Bi_2X_9$ perovskites under the pressures from 0 GPa to 40 GPa (**d**).

Based on the semiconductor theory, analyzing the band structure and the DOS very closely, the Fermi level is important for establishing the possible applications of a material in the photoelectric and photovoltaic fields. We therefore calculated the band structure near the Fermi level (from −5 eV to +5 eV) under different pressures. The calculated bandgaps at a pressure of 0 GPa of the $Cs_3Bi_2I_9$, $Cs_3Bi_2Br_9$, and $Cs_3Bi_2Cl_9$ are 2.38, 2.60, and 3.08 eV, respectively. The scissor value approach was used to establish the band structure of the $Cs_3Bi_2X_9$ perovskites in order to obtain the accurate value for the $Cs_3Bi_2X_9$ perovskites when they reached the optimal bandgap of the Shockley–Queisser theory and the transition from semiconductor to metal; this methodology overcame the limitations of the GGA–PBE calculation method and has already been applied in the study of the photoelectric properties of the $CsSnCl_3$ perovskite at HPs [40]. Many experimental studies have been conducted regarding the bandgaps of the $Cs_3Bi_2I_9$, $Cs_3Bi_2Br_9$, and $Cs_3Bi_2Cl_9$ perovskites. Among these, Daniel R. Gamelin et al. synthesized $Cs_3Bi_2X_9$ perovskites nanocrystals via the thermal injection method, and the bandgaps of the $Cs_3Bi_2I_9$, $Cs_3Bi_2Br_9$, and $Cs_3Bi_2Cl_9$ perovskites were measured as 2.07, 2.76, and 3.26 eV, respectively [43]. Therefore, the scissors values of −0.31eV, 0.16eV, and 0.18eV were used for the $Cs_3Bi_2I_9$, $Cs_3Bi_2Br_9$, and $Cs_3Bi_2Cl_9$ perovskites, respectively.

Figure 3 shows the change in the band structure of the $Cs_3Bi_2I_9$ perovskite under the pressures of 0 (a), 4 (b), 10 (c), and 40 GPa (d). Without external pressure, the conduction band minimum (CBM) and the valence band maximum (VBM) of $Cs_3Bi_2I_9$ perovskite are located at the Γ- and M-points, respectively. We found the $Cs_3Bi_2I_9$ perovskite to be an indirect bandgap material, which is consistent with the existing literature [44]. The semiconductor with the optimized band gap energy of 1.34 eV is critical to achieve the efficiency limit of 33.7% based on the Shockley–Queisser theory [34]. In Figure 3, it can be seen that the bandgap of the $Cs_3Bi_2I_9$ perovskite decreases sharply with the increase in pressure and reaches its optimal bandgap value given by the Shockley–Queisser theory at 2–3 GPa. In addition, with the high pressure further increasing, the CBM continues to decrease and

the VBM moves from the M-point to near the K-point. The $Cs_3Bi_2I_9$ perovskite completed the transition from semiconductor to metal at 17.3 GPa, and this finding indicated that HP is an effective means to induce the semiconductor–metal transition. The band structure of the $Cs_3Bi_2Br_9$ perovskite under the pressures of 0 (a), 4 (b), 10 (c), and 40 GPa (d) is presented in Figure 4. As can be seen from Figure 4, when the pressure is 0 GPa (a), the calculated band structure of the $Cs_3Bi_2Br_9$ perovskite is consistent with the results reported by Brent C. Melot et al. [45] They found a low-lying 2.52 eV indirect transition as well as a slightly larger direct gap of 2.64 eV, which are essentially in agreement with our calculated results. This structural characteristic becomes increasingly evident with the increase in pressure. The $Cs_3Bi_2Br_9$ perovskite reaches the optimal bandgap given by the Shockley–Queisser theory at 21–26 GPa, which means that the electron transitions from the valence band to conduction band become easier. Figure 5a–d shows the change of the band structure of $Cs_3Bi_2Cl_9$ perovskite with HP. The $Cs_3Bi_2Cl_9$ perovskite reaches the optimal bandgap in the range of 25–29 GPa; it is an indirect bandgap material. The CBM is at the Γ- point, and the VBM moves from the Γ-point to the Y-point, which is consistent with the results reported previously [41]. However, it was found that the $Cs_3Bi_2Br_9$ and $Cs_3Bi_2Cl_9$ perovskites did not metallize under HP despite the pressure reaching 40 GPa in both cases, which may be related to their unique structure. The bandgap changes in the $Cs_3Bi_2X_9$ perovskites under a range of HP (0, 2, 4, 6, 8, 10, 20, 30, and 40 GPa) are shown in Supplementary Figures S1–S3.

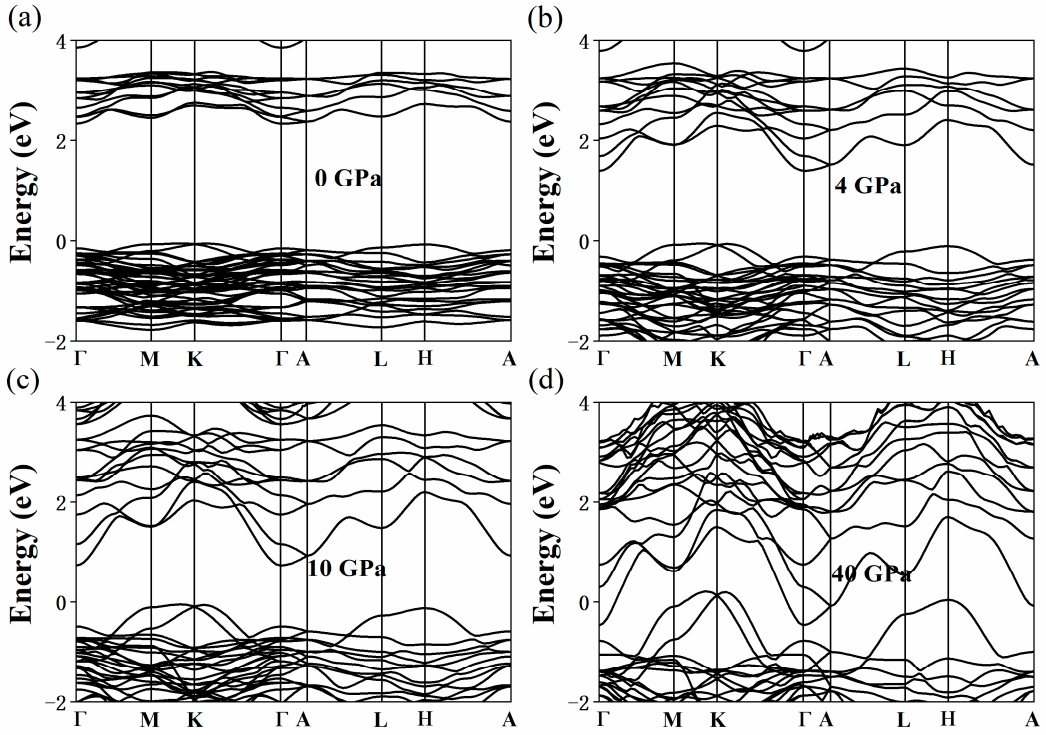

Figure 3. Calculated band structure of the $Cs_3Bi_2I_9$ perovskite under the pressures of 0 (**a**), 4 (**b**), 10 (**c**), and 40 GPa (**d**).

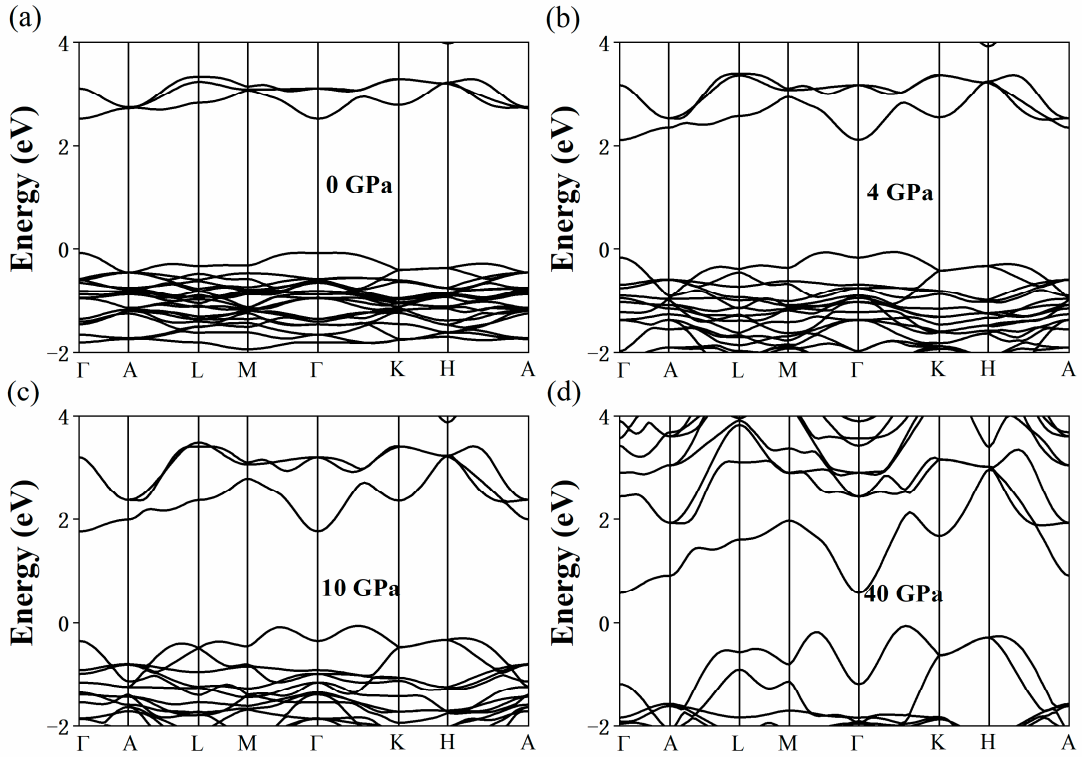

Figure 4. Calculated band structure of the $Cs_3Bi_2Br_9$ perovskite under the pressures of 0 (**a**), 4 (**b**), 10 (**c**), and 40 GPa (**d**).

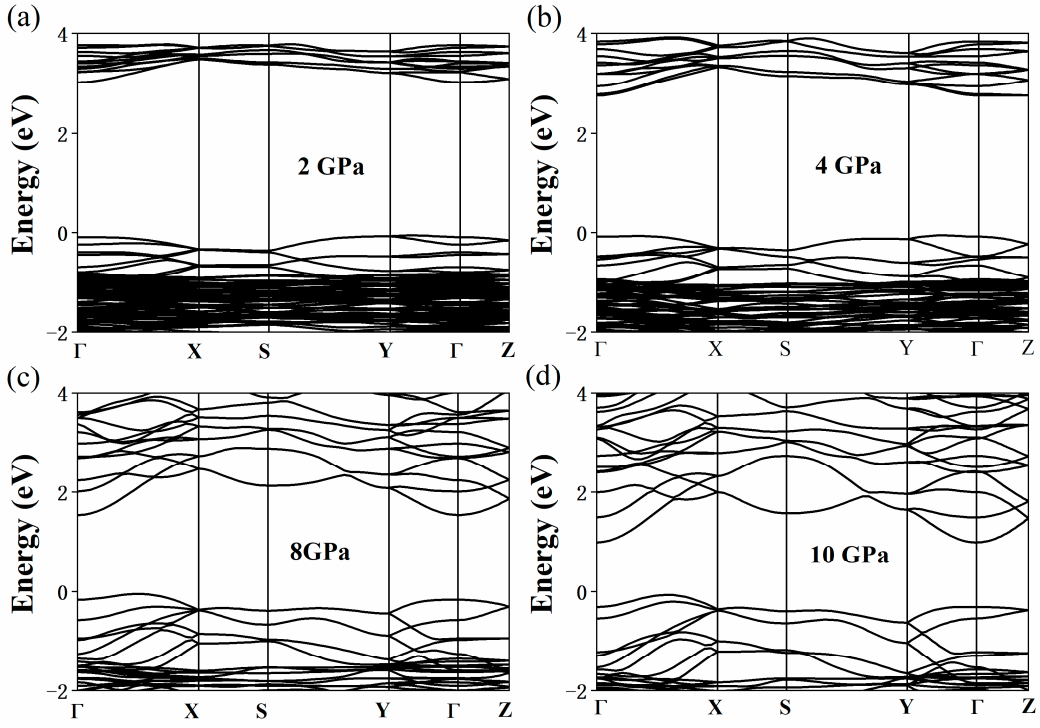

Figure 5. Calculated band structure of the $Cs_3Bi_2Cl_9$ perovskite under the pressures of 0 (**a**), 4 (**b**), 10 (**c**), and 40 GPa (**d**).

Figure 6 shows the changes in the bandgaps of the $Cs_3Bi_2I_9$, $Cs_3Bi_2Br_9$, and $Cs_3Bi_2Cl_9$ perovskites under HP. It can be seen that the bandgap of the $Cs_3Bi_2X_9$ perovskites decreases with the increase in pressure (Figure 6a); the bandgap of the $Cs_3Bi_2I_9$ perovskite takes a negative value, which is a typical indicator of metallic behavior. Figure 6b shows the change in the bandgap of the $Cs_3Bi_2X_9$ perovskites after using the scissor values under

HP. When the pressure is varied from 0 to 40 GPa, the bandgap differences of the $Cs_3Bi_2I_9$, $Cs_3Bi_2Br_9$, and $Cs_3Bi_2Cl_9$ perovskites are 3.05, 1.95, and 2.39 eV, respectively. It was found that with the increase in dimension, the bandgap differences of the $Cs_3Bi_2I_9$, $Cs_3Bi_2Br_9$, and $Cs_3Bi_2Cl_9$ perovskites decrease in turn, which indicates that the bandgap of the $Cs_3Bi_2X_9$ perovskites depends on dimension.

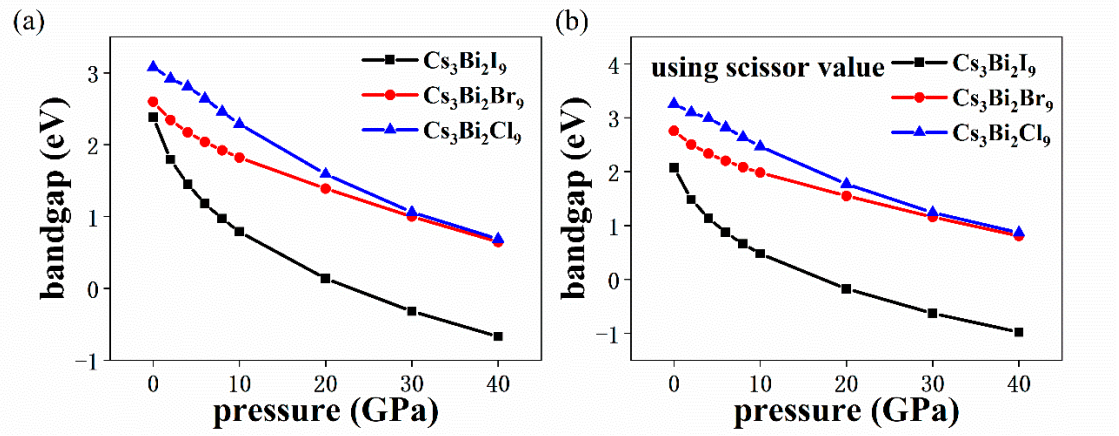

Figure 6. Calculated bandgap of the $Cs_3Bi_2X_9$ perovskites as a function of pressure (from 0 GPa to 40 GPa) (**a**). Changes in the bandgap of the $Cs_3Bi_2X_9$ perovskite after using the scissor values under HP (**b**). The black, red, and blue lines represent the $Cs_3Bi_2I_9$, $Cs_3Bi_2Br_9$, and $Cs_3Bi_2Cl_9$ perovskites, respectively.

To explain the dimension-dependent bandgap of the $Cs_3Bi_2X_9$, we investigate the construction of these perovskites. Based upon the primitive cell of $Cs_3Bi_2I_9$, $Cs_3Bi_2Br_9$ and the $Cs_3Bi_2Cl_9$ perovskites, the $2 \times 2 \times 1$, $2 \times 2 \times 2$, and $3 \times 1 \times 1$ supercells are shown in Figure 7a–c, respectively. In Figure 7d, ΔL represents the difference in the lattice constants of the $Cs_3Bi_2X_9$ perovskites between 0 and 40 GPa along the a, b, and c coordinate axes. In general, for centrosymmetric perovskites, the ΔL values along the *a*- (ΔL_a), *b*- (ΔL_b), and *c*- (ΔL_c) axes are equal under HP. However, we found that ΔL_a, ΔL_b, and ΔL_c for the double perovskites were not equal; in other words, ΔL is anisotropic along the *a*-, *b*-, and *c*-axes. The ΔL_a, ΔL_b, and ΔL_c values for the $Cs_3Bi_2I_9$ perovskite (zero-dimensional) are 1.57, 1.57, and 5.2. It can be seen that ΔL_c is much larger than both ΔL_a and ΔL_b. The reason for this difference is that the $Bi_2I_9^{3-}$ frame of the double-perovskite is continuous along the *a*- and *b*-axes but not along the c-axis. Along the c-axis, only the Cs^+ atoms are above or below the $Bi_2I_9^{3-}$ frame, which indicates that the change in the lattice constant along the c-axis is bigger than that observed along the *a*- and *b*-axes when the zero-dimensional $Cs_3Bi_2I_9$ perovskite is placed under HP.

The previous analysis shows that if the double-perovskite frame expands regularly in one direction, the ΔL in this direction will be smaller than in the other directions under HP. This indicates that the lattice constants of the $Cs_3Bi_2X_9$ perovskites are dependent on dimension. In general, the lattice constant and the bandgap decrease as the pressure increases [34]. It has also been found that the changes in the bandgap of the zero-dimensional $Cs_3Bi_2I_9$, one-dimensional $Cs_3Bi_2Cl_9$, and two-dimensional $Cs_3Bi_2Br_9$ perovskites between 40 and 0 GPa are 3.05, 2.39, and 1.95 eV, respectively. These results illustrate that the bandgaps of the $Cs_3Bi_2X_9$ perovskites are also dependent upon dimension; that is, the changes in the bandgap decrease gradually as the dimension increased from zero to two under the same pressure.

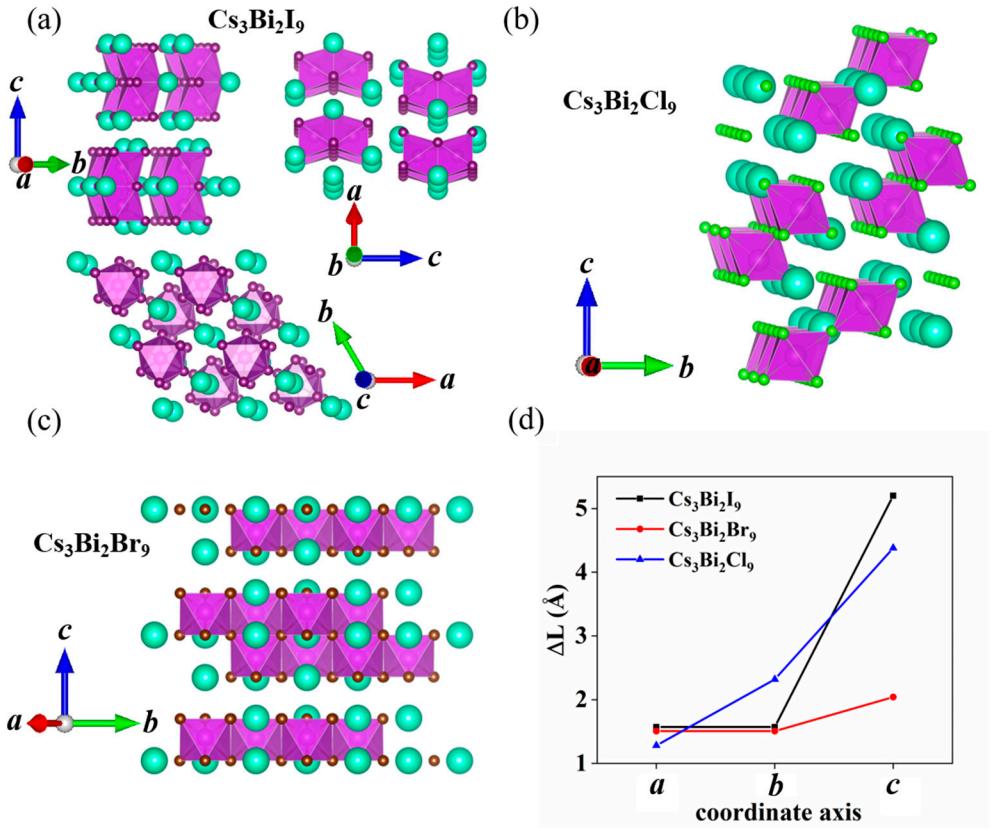

Figure 7. Crystal structure of the zero-dimensional $Cs_3Bi_2I_9$ (**a**), one-dimensional $Cs_3Bi_2Cl_9$ (**b**), and two-dimensional $Cs_3Bi_2Br_9$ (**c**). Difference in the lattice constants of the $Cs_3Bi_2X_9$ perovskites for the pressures between 0 and 40 GPa along the a, b, and c axes (**d**). The black, red, and blue lines represent $Cs_3Bi_2I_9$, $Cs_3Bi_2Br_9$, and $Cs_3Bi_2Cl_9$, respectively.

The partial density of states (PDOS) of the zero-dimensional $Cs_3Bi_2I_9$ (a), one-dimensional $Cs_3Bi_2Cl_9$ (b), and two-dimensional $Cs_3Bi_2Br_9$ (c) perovskites were shown in Figure 8. It can be seen that the VBM of the $Cs_3Bi_2X_9$ perovskites is dominated by p-X states, whereas the CBM is dominated by the p-Bi and p-X states (see Figure 8a–c). The changes in the DOS under HP are shown in Figure 8d–f. It is clear that many valence bands in the $Cs_3Bi_2X_9$ perovskites move to a deep level, and the conduction bands approach to the FE with an increase in pressure for $Cs_3Bi_2X_9$ perovskites; the shift of the conduction bands under the HP will induce the changes in the bandgap. In contrast to those of the $Cs_3Bi_2Br_9$ and $Cs_3Bi_2Cl_9$ perovskites, the forbidden band width of the $Cs_3Bi_2I_9$ gradually decreases and subsequently disappears, which indicates that the $Cs_3Bi_2I_9$ perovskite is no longer a semiconductor; it becomes a metal at 17.3 GPa. This conclusion is agreement with the calculated results for the band structure.

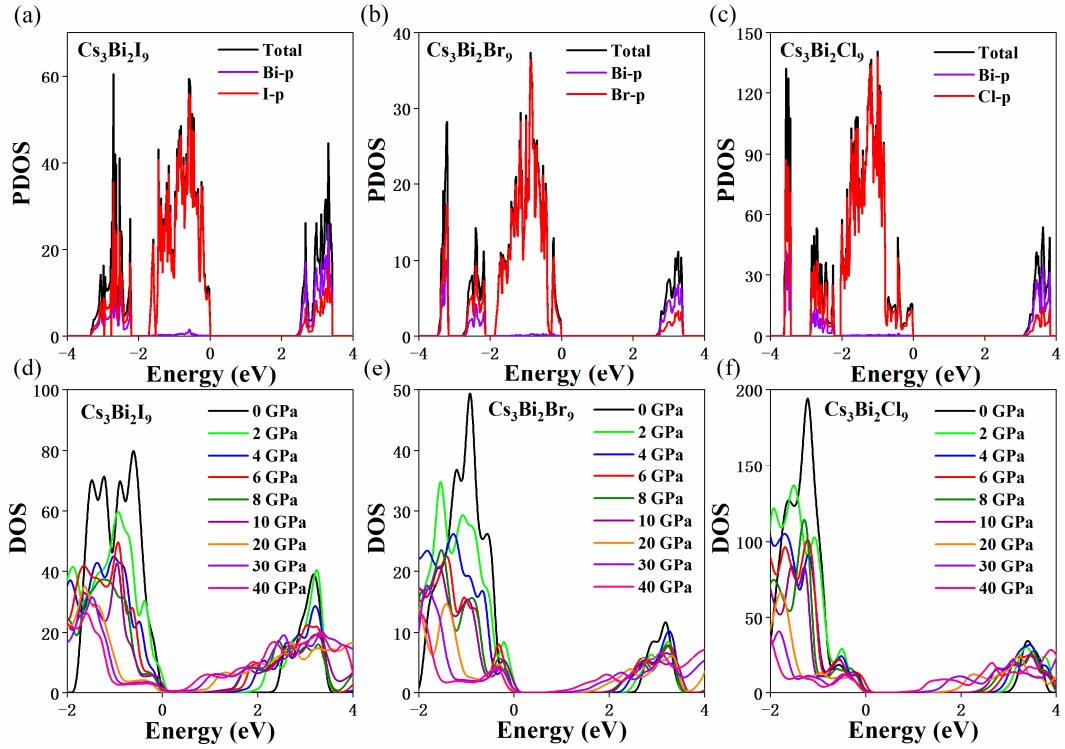

Figure 8. Partial state of density (PDOS) of $Cs_3Bi_2I_9$ (**a**), $Cs_3Bi_2Br_9$ (**b**), and $Cs_3Bi_2Cl_9$ (**c**). the VBM of the $Cs_3Bi_2X_9$ perovskites (X = I, Br, and Cl) is dominated by the p-X states, and the CBM is dominated by the p-Bi and p-X states. Calculated density of states (DOS) of the $Cs_3Bi_2I_9$ (**d**), $Cs_3Bi_2Br_9$ (**e**), and $Cs_3Bi_2Cl_9$ (**f**) under the pressures from 0 to 40 GPa.

A large absorption coefficient is of great significance in photoelectric and photovoltaic applications. Such a property improves the PCE of solar cells and the luminous efficiency. The absorption coefficient is usually described by the dielectric function according to the following expression [46]:

$$\alpha = 2\omega \left[\frac{\left(\varepsilon_1^2(\omega) + \varepsilon_2^2(\omega)\right)^{1/2} - \varepsilon_1(\omega)}{2} \right]^{1/2}$$

where the ω is the frequency of light, and ε_1 and ε_2 are the real and imaginary parts of the dielectric function, respectively. The calculated ε_1 and ε_2 values of the $Cs_3Bi_2X_9$ perovskites are presented in Supplementary Figures S4–S6 along the *a*-, *b*-, and *c*-axes. The static dielectric function of the $Cs_3Bi_2X_9$ perovskites increases gradually with increasing pressure from 0 to 40 GPa. The ε_2 value is closely related to the optical absorption and usually used to describe the absorption behavior of materials.

The calculated absorption coefficients of the $Cs_3Bi_2X_9$ perovskites are shown in Figures 9 and 10 along the *a*-, *b*-, and *c*-axes. It was found that the $Cs_3Bi_2I_9$ perovskite has the same absorption coefficient along the a- and b-axes with the increase in pressure, as is the case for the $Cs_3Bi_2Br_9$ perovskite. The absorption coefficients of the $Cs_3Bi_2Cl_9$ perovskite are unequable along the *a*-, *b*-, and *c*-axes under HP. The ΔL value of the $Cs_3Bi_2X_9$ perovskites in Figure 7d is consistent with these behaviors, which suggests that the changes in the structure of the $Cs_3Bi_2X_9$ perovskites under HP will affect the optical properties considerably. The $Cs_3Bi_2X_9$ perovskites exhibit a redshift with the increase in pressure, which indicates that the $Cs_3Bi_2X_9$ can absorb the low-energy photons. Moreover, the absorption coefficients of the $Cs_3Bi_2X_9$ perovskites increase gradually in the ultraviolet region as the pressure increases from 0 to 40 GPa. It was also found that the $Cs_3Bi_2X_9$ perovskites have a large absorption coefficient in the visible region (on the order of 10^5 cm^{-1}). Therefore,

the $Cs_3Bi_2X_9$ perovskites are an attractive candidate in applications of photoelectric and photovoltaic devices.

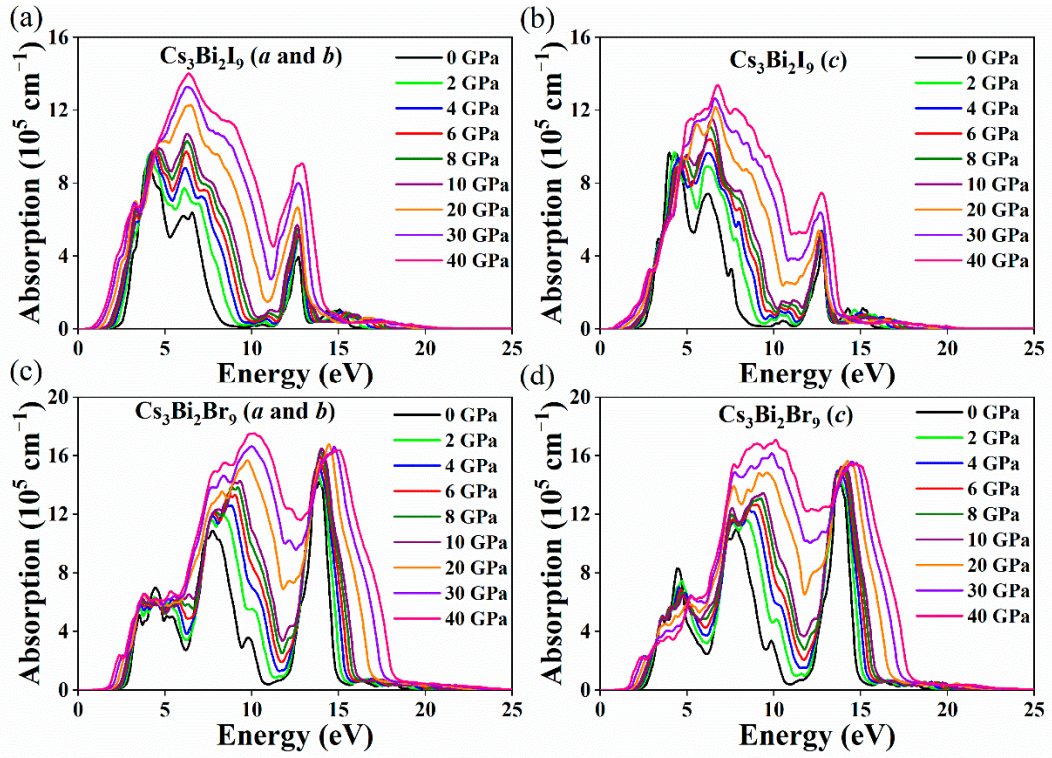

Figure 9. Absorption coefficients of the $Cs_3Bi_2I_9$ along the *a*- and *b*-axes (**a**), $Cs_3Bi_2I_9$ along *c*-axis (**b**), $Cs_3Bi_2Br_9$ along the *a*- and *b*-axes (**c**), and $Cs_3Bi_2Br_9$ along the *c*-axis (**d**) as a function of the pressure (from 0 to 40 GPa).

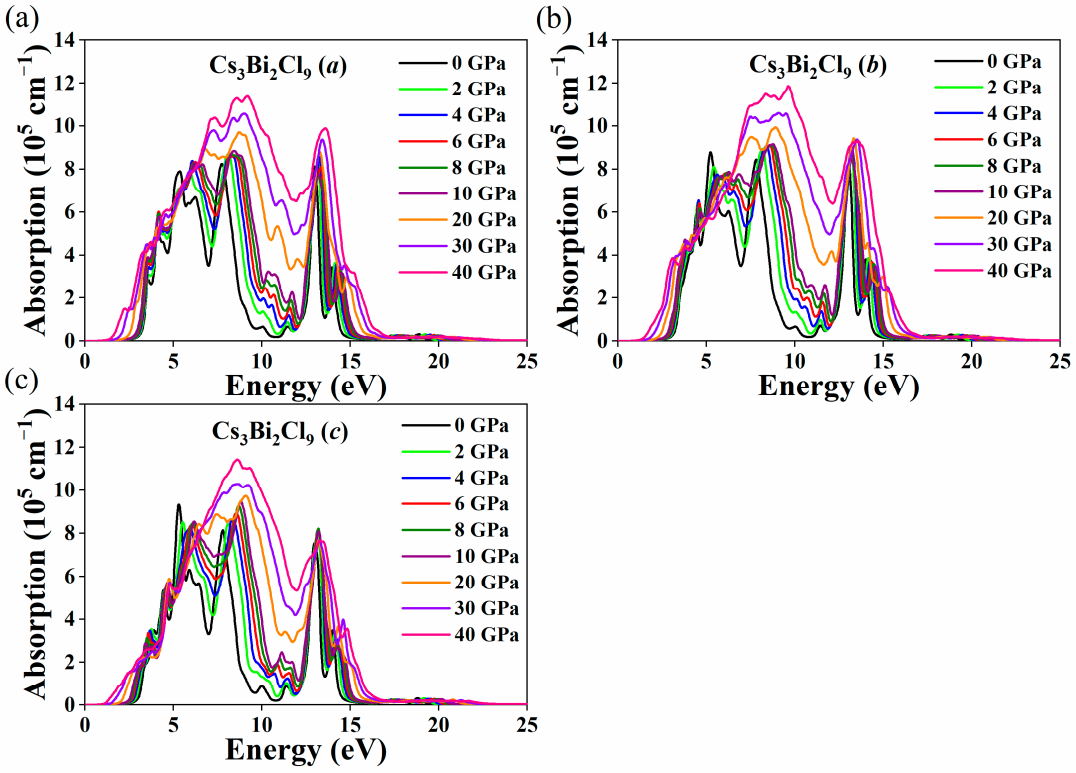

Figure 10. Absorption coefficients of $Cs_3Bi_2Cl_9$ along the *a*-axis (**a**), along the *b*-axis (**b**), and along the *c*-axis (**c**) as a function of the pressure (from 0 to 40 GPa).

4. Conclusions

In summary, we investigated the lattice constants, band structure, DOS, and optical absorption of the cesium bismuth iodide $Cs_3Bi_2X_9$ (X = I, Br and Cl) perovskites under HP by using the DFT. It was found that the optimal bandgap of the Shockley–Queisser theory for the $Cs_3Bi_2I_9$, $Cs_3Bi_2Br_9$, and $Cs_3Bi_2Cl_9$ perovskites can be obtained at 2–3 GPa, 21–26 GPa, and 25–29 GPa, respectively. The changes in the bandgap of $Cs_3Bi_2I_9$, $Cs_3Bi_2Br_9$, and $Cs_3Bi_2Cl_9$ perovskites are 3.05, 1.95, and 2.39 eV under a pressure of 40 GPa, respectively. The $Cs_3Bi_2I_9$ perovskite was found to transform from a semiconductor into a metal at 17.3 GPa. Furthermore, the dimension-dependent lattice constants, unit-cell volumes, and bandgaps of the $Cs_3Bi_2X_9$ perovskites were studied. Our calculations show that HP is an effective way to tune the photovoltaic and optoelectronic properties of the $Cs_3Bi_2X_9$ perovskites by modifying the crystal structure, which provides a promising method for material design and applications.

Supplementary Materials: The following are available online at https://www.mdpi.com/article/10.3390/nano11102712/s1. Table S1: Summarized bandgap values of $Cs_3Bi_2X_9$ perovskites under high pressure; Figure S1: Calculated band structures of the $Cs_3Bi_2I_9$ perovskite under the different pressures (**a**–**i**); Figure S2: Calculated band structures of the $Cs_3Bi_2Br_9$ perovskite under the different pressures (**a**–**i**); Figure S3: Calculated band structures of the $Cs_3Bi_2Cl_9$ perovskite under the different pressures (**a**–**i**); Figure S4: Real part of the dielectric function of the $Cs_3Bi_2I_9$ perovskite along the *a*- and *b*-axes (**a**), and the *c*-axis (**b**) as a function of pressure (from 0 to 40 GPa). Imaginary part of the dielectric function of the $Cs_3Bi_2I_9$ perovskite along the *a*- and *b*-axes (**c**), and along the *c*-axis) (**d**) as a function of pressure (from 0 to 40 GPa); Figure S5: Real part of the dielectric function of the $Cs_3Bi_2Br_9$ perovskite along the *a*- and *b*-axes (**a**), and the *c*-axis (**b**) as a function of pressure (from 0 to 40 GPa). Imaginary part of the dielectric function of the $Cs_3Bi_2Br_9$ perovskite along the *a*- and *b*-axes (**c**), and along the *c*-axis) (**d**) as a function of pressure (from 0 to 40 GPa); Figure S6: Real part of the dielectric function of the $Cs_3Bi_2Cl_9$ perovskite along the *a*-axis (**a**), along the *b*-axis (**b**), and along the *c*-axis (**c**) as a function of pressure (from 0 to 40 GPa). Imaginary part of the dielectric function of the $Cs_3Bi_2Cl_9$ perovskite along the *a*-axis (**d**), along the *b*-axis (**e**), and along the *c*-axis (**f**) as a function of pressure (from 0 to 40 GPa).

Author Contributions: Conceptualization, G.X., Y.W. and H.M.; theoretical calculation, G.X., Y.W., M.Z. and C.C.; writing—original draft preparation, G.X., M.Z. and H.M.; writing—review and editing, H.M. and J.L.; supervision, funding acquisition, J.L., C.C. and H.M. All authors have read and agreed to the published version of the manuscript.

Funding: This work was funded by the Natural Science Foundation of Shandong Province (Nos. ZR2020MA081, ZR2019MA037, and ZR2018BA031). This work also received the financial support from by the National Natural Science Foundation of China (NFSC) (No. 11904212) and the Research Leader Program of Jinan Science and Technology Bureau (No. 2019GXRC061).

Institutional Review Board Statement: Not applicable.

Informed Consent Statement: Not applicable.

Data Availability Statement: Data are contained within the article.

Conflicts of Interest: The authors declare no conflict of interest.

References

1. Liu, X.; Xu, W.; Bai, S.; Jin, Y.; Wang, J.; Friend, R.H.; Gao, F. Metal halide perovskites for light-emitting diodes. *Nat. Mater.* **2021**, *20*, 10–21. [CrossRef]
2. Jia, Y.; Kerner, R.A.; Grede, A.J.; Rand, B.P.; Giebink, N.C. Continuous-wave lasing in an organic-inorganic lead halide semiconductor. *Nat. Photonics* **2017**, *11*, 784–788. [CrossRef]
3. Lin, K.; Xing, J.; Quan, L.; Arquer, F.P.G.; Gong, X.; Lu, J.; Xie, L.; Zhao, W.; Zhang, D.; Yan, C.; et al. Perovskite light-emitting diodes with external quantum efficiency exceeding 20 per cent. *Nature* **2018**, *562*, 245–248. [CrossRef]
4. Chen, B.; Baek, S.W.; Hou, Y.; Aydin, E.; Bastiani, M.D.; Scheffel, B.; Proppe, A.; Huang, Z.; Wei, M.; Wang, Y.; et al. Enhanced optical path and electron diffusion length enable high-efficiency perovskite tandems. *Nat. Commun.* **2020**, *11*, 1–9. [CrossRef]

5. Leng, K.; Abdelwahab, I.; Verzhbitskiy, I.; Telychko, M.; Chu, L.; Fu, W.; Chi, X.; Guo, N.; Chen, Z.; Chen, Z.; et al. Molecularly thin two-dimensional hybrid perovskites with tunable optoelectronic properties due to reversible surface relaxation. *Nat. Mater.* **2018**, *17*, 908–914. [CrossRef]
6. Shao, H.; Bai, X.; Cui, H.; Pan, G.; Jing, P.; Qu, S.; Zhu, J.; Zhai, Y.; Dong, B.; Song, H. White light emission in Bi^{3+}/Mn^{2+} ion co-doped $CsPbCl_3$ perovskite nanocrystals. *Nanoscale* **2018**, *10*, 1023–1029. [CrossRef]
7. Yang, S.; Chen, S.; Mosconi, E.; Fang, Y.; Xiao, X.; Wang, C.; Zhou, Y.; Yu, Z.; Zhao, J.; Gao, Y.; et al. Stabilizing halide perovskite surfaces for solar cell operation with wide-bandgap lead oxysalts. *Science* **2019**, *365*, 473–478. [CrossRef]
8. Zhou, L.; Guo, X.; Lin, Z.; Ma, J.; Su, J.; Hu, Z.; Zhang, C.; Liu, S.; Chang, J.; Hao, Y. Interface engineering of low temperature processed all-inorganic $CsPbI_2Br$ perovskite solar cells toward PCE exceeding 14%. *Nano Energy* **2019**, *60*, 583–590. [CrossRef]
9. Kojima, A.; Teshima, K.; Shirai, Y.; Miyasaka, T. Organometal Halide Perovskites as Visible-Light Sensitizers for Photovoltaic Cells. *J. Am. Chem. Soc.* **2009**, *131*, 6050–6051. [CrossRef]
10. Tang, S.; Bing, J.; Zheng, J.; Tang, J.; Li, Y.; Mayyas, M.; Cho, Y.; Jones, T.W.; Yang, T.C.J.; Yuan, L.; et al. Complementary bulk and surface passivations for highly efficient perovskite solar cells by gas quenching. *Cell Rep. Phys. Sci.* **2021**, *2*, 100511. [CrossRef]
11. Yang, B.; Chen, J.; Hong, F.; Mao, X.; Zheng, K.; Yang, S.; Li, Y.; Pullerits, T.; Deng, W.; Han, K. Lead-Free, Air-Stable All-Inorganic Cesium Bismuth Halide Perovskite Nanocrystals. *Angew. Chem. Int. Ed.* **2017**, *56*, 12471–12475. [CrossRef]
12. Leng, M.; Yang, Y.; Zeng, K.; Chen, Z.; Tan, Z.; Li, S.; Li, J.; Xu, B.; Li, D.; Hautzinger, M.P.; et al. All-Inorganic Bismuth-Based Perovskite Quantum Dots with Bright Blue Photoluminescence and Excellent Stability. *Adv. Funct. Mater.* **2017**, *28*, 1704446. [CrossRef]
13. Lou, Y.; Fang, M.; Chen, J.; Zhao, Y. Formation of highly luminescent cesium bismuth halide perovskite quantum dots tuned by anion exchange. *Chem. Commun.* **2018**, *54*, 3779–3782. [CrossRef]
14. Cao, Y.; Zhang, Z.; Li, L.; Zhang, J.; Zhu, J. An Improved Strategy for High-Quality Cesium Bismuth Bromine Perovskite Quantum Dots with Remarkable Electrochemiluminescence Activities. *Anal. Chem.* **2019**, *91*, 8607–8614. [CrossRef] [PubMed]
15. Ma, Z.; Shi, Z.; Wang, L.; Zhang, F.; Wu, D.; Yang, D.; Chen, X.; Zhang, Y.; Shan, C.; Li, X. Water-induced fluorescence enhancement of lead-free cesium bismuth halide quantum dots by 130% for stable white light-emitting devices. *Nanoscale* **2020**, *12*, 3637–3645. [CrossRef]
16. Ji, Z.; Liu, Y.; Li, W.; Zhao, C.; Mai, W. Reducing current fluctuation of $Cs_3Bi_2Br_9$ perovskite photodetectors for diffuse reflection imaging with wide dynamic range. *Sci. Bull.* **2020**, *65*, 1371–1379. [CrossRef]
17. Gu, J.; Yan, G.; Lian, Y.; Mu, Q.; Jin, H.; Zhang, Z.; Deng, Z.; Peng, Y. Bandgap engineering of a lead-free defect perovskite $Cs_3Bi_2I_9$ through trivalent doping of Ru^{3+}. *RSC Adv.* **2018**, *8*, 25802–25807. [CrossRef]
18. Han, J.; Le, Q.V.; Kim, H.; Lee, Y.J.; Lee, D.E.; Im, I.H.; Lee, M.K.; Kim, S.J.; Kim, J.; Kwak, K.J.; et al. Lead-Free Dual-Phase Halide Perovskites for Preconditioned Conducting-Bridge Memory. *Small* **2020**, *16*, 2003225. [CrossRef]
19. Liu, D.; Yu, B.; Liao, M.; Jin, Z.; Zhou, L.; Zhang, X.; Wang, F.; He, H.; Gatti, T.; He, Z. Self-powered and broadband lead-free inorganic perovskite photodetector with high stability. *ACS Appl. Mater. Interfaces* **2020**, *12*, 30530–30537. [CrossRef]
20. Li, W.; Wang, X.; Liao, J.; Jiang, Y.; Kuang, D. Enhanced On–Off Ratio Photodetectors Based on Lead-Free $Cs_3Bi_2I_9$ Single Crystal Thin Films. *Adv. Funct. Mater.* **2020**, *30*, 1909701. [CrossRef]
21. Khadka, D.B.; Shirai, Y.; Yanagida, M.; Miyano, K. Tailoring the film morphology and interface band offset of caesium bismuth iodide-based Pb-free perovskite solar cells. *J. Mater. Chem. C* **2019**, *7*, 8335–8343. [CrossRef]
22. Johansson, M.B.; Philippe, B.; Banerjee, A.; Phuyal, D.; Mukherjee, S.; Chakraborty, S.; Cameau, M.; Zhu, H.; Ahuja, R.; Boschloo, G.; et al. Cesium Bismuth Iodide Solar Cells from Systematic Molar Ratio Variation of CsI and BiI_3. *Inorg. Chem.* **2019**, *58*, 12040–12052. [CrossRef]
23. Ge, S.; Guan, X.; Wang, Y.; Lin, C.; Cui, Y.; Huang, Y.; Zhang, X.; Zhang, R.; Yang, X.; Wu, T. Low-Dimensional Lead-Free Inorganic Perovskites for Resistive Switching with Ultralow Bias. *Adv. Funct. Mater.* **2020**, *30*, 2002110. [CrossRef]
24. Zhang, Y.; Liu, Y.; Xu, Z.; Ye, H.; Yang, Z.; You, J.; Liu, M.; He, Y.; Kanatzidis, M.G.; Liu, S. Nucleation-controlled growth of superior lead-free perovskite $Cs_3Bi_2I_9$ single-crystals for high-performance X-ray detection. *Nat. Commun.* **2020**, *11*, 1–11.
25. Hu, Y.; Zhang, S.; Miao, X.; Su, L.; Bai, F.; Qiu, T.; Liu, J.; Yuan, G. Ultrathin $Cs_3Bi_2I_9$ Nanosheets as an Electronic Memory Material for Flexible Memristors. *Adv. Mater. Interfaces* **2017**, *4*, 1700131. [CrossRef]
26. Liang, J.; Fang, Q.; Wang, H.; Xu, R.; Jia, S.; Guan, Y.; Ai, Q.; Gao, G.; Guo, H.; Shen, K.; et al. Perovskite-Derivative Valleytronics. *Adv. Mater.* **2020**, *32*, 2004111. [CrossRef]
27. Samanta, D.; Saha, P.; Ghosh, B.; Chaudhary, S.P.; Bhattacharyya, S.; Chatterjee, S.; Mukherjee, G.D. Pressure-Induced Emergence of Visible Luminescence in Lead Free Halide Perovskite $Cs_3Bi_2Br_9$: Effect of Structural Distortion. *J. Phys. Chem. C* **2021**, *125*, 3432–3440. [CrossRef]
28. Nagaoka, Y.; Hills-Kimball, K.; Tan, R.; Li, R.; Wang, Z.; Chen, O. Nanocube Superlattices of Cesium Lead Bromide Perovskites and Pressure-Induced Phase Transformations at Atomic and Mesoscale Levels. *Adv. Mater.* **2017**, *29*, 1606666. [CrossRef]
29. Lü, X.; Wang, Y.; Stoumpos, C.C.; Hu, Q.; Guo, X.; Chen, H.; Yang, L.; Smith, J.S.; Yang, W.; Zhao, Y.; et al. Enhanced Structural Stability and Photo Responsiveness of $CH_3NH_3SnI_3$ Perovskite via Pressure-Induced Amorphization and Recrystallization. *Adv. Mater.* **2016**, *28*, 8663–8668. [CrossRef]
30. Postorino, P.; Malavasi, L. Pressure-Induced Effects in Organic−Inorganic Hybrid Perovskites. *J. Phys. Chem. Lett.* **2017**, *8*, 2613–2622. [CrossRef]

31. Szafranski, M.; Katrusiak, A. Mechanism of Pressure-Induced Phase Transitions, Amorphization, and Absorption-Edge Shift in Photovoltaic Methylammonium Lead Iodide. *J. Phys. Chem. Lett.* **2016**, *7*, 3458–3466. [CrossRef] [PubMed]
32. Zhang, L.; Zeng, Q.; Wang, K. Pressure-Induced Structural and Optical Properties of Inorganic Halide Perovskite $CsPbBr_3$. *J. Phys. Chem. Lett.* **2017**, *8*, 3752–3758. [CrossRef] [PubMed]
33. Wang, Y.; Lü, X.; Yang, W.; Wen, T.; Yang, L.; Ren, X.; Wang, L.; Lin, Z.; Zhao, Y. Pressure-Induced Phase Transformation, Reversible Amorphization, and Anomalous Visible Light Response in Organolead Bromide Perovskite. *J. Am. Chem. Soc.* **2015**, *137*, 11144–11149. [CrossRef] [PubMed]
34. Zhang, L.; Liu, C.; Wang, L.; Liu, C.; Wang, K.; Zou, B. Pressure-Induced Emission Enhancement, Band Gap Narrowing and Metallization of Halide Perovskite $Cs_3Bi_2I_9$. Angew. *Chem. Int. Ed.* **2018**, *57*, 11213–11217. [CrossRef]
35. Geng, T.; Wei, S.; Zhao, W.; Ma, Z.; Fu, R.; Xiao, G.; Zou, B. Insight into the structure–property relationship of two-dimensional lead-free halide perovskite $Cs_3Bi_2Br_9$ nanocrystals under pressure. *Inorg. Chem. Front.* **2021**, *8*, 1410–1415. [CrossRef]
36. Kresse, G.; Furthmüller, J. Efficient iterative schemes for ab initio total-energy calculations using a plane-wave basis set. *Phys. Rev. B* **1996**, *54*, 11169. [CrossRef] [PubMed]
37. Blochl, P.E. Projector augmented-wave method. *Phys. Rev. B* **1994**, *50*, 17953–17979. [CrossRef] [PubMed]
38. Perdew, J.P.; Burke, K.; Ernzerhof, M. Generalized gradient approximation made simple. *Phys. Rev. Lett.* **1996**, *77*, 3865. [CrossRef] [PubMed]
39. Monkhorst, H.J.; Pack, J.D. Special points for Brillouin-zone integrations. *Phys. Rev. B* **1976**, *13*, 5188–5192. [CrossRef]
40. Islam, J.; Hossain, A. Semiconducting to metallic transition with outstanding optoelectronic properties of $CsSnCl_3$ perovskite under pressure. *Sci. Rep.* **2020**, *10*, 1–11. [CrossRef]
41. Morgan, E.E.; Mao, L.; Teicher, S.M.L.; Wu, G.; Seshadri, R. Tunable Perovskite-Derived Bismuth Halides: $Cs_3Bi_2(Cl_{1-x}I_x)_9$. *Inorg. Chem.* **2020**, *59*, 3387–3393. [CrossRef] [PubMed]
42. Khoram, P.; Brittman, S.; Dzik, W.I.; Reek, J.N.H.; Garnett, E.C. Growth and Characterization of PDMS-Stamped Halide Perovskite Single Microcrystals. *J. Phys. Chem. C* **2016**, *120*, 6475–6481. [CrossRef]
43. Creutz, S.E.; Liu, H.; Kaiser, M.E.; Li, X.; Gamelin, D.R. Structural Diversity in Cesium Bismuth Halide Nanocrystals. *Chem. Mater.* **2019**, *31*, 4685–4697. [CrossRef]
44. Ghosh, B.; Chakraborty, S.; Wei, H.; Guet, C.; Li, S.; Mhaisalkar, S.; Mathews, N. Poor Photovoltaic Performance of $Cs_3Bi_2I_9$: An Insight through First Principles Calculations. *J. Phys. Chem. C* **2017**, *121*, 17062–17067. [CrossRef]
45. Bass, K.K.; Estergreen, L.; Savory, C.N.; Buckeridge, J.; Scanlon, D.O.; Djurovich, P.I.; Bradforth, S.E.; Thompson, M.E.; Melot, B.C. Vibronic Structure in Room Temperature Photoluminescence of the Halide Perovskite $Cs_3Bi_2Br_9$. *Inorg. Chem.* **2017**, *56*, 42–45. [CrossRef] [PubMed]
46. Xiang, G.; Wu, Y.; Li, Y.; Cheng, C.; Leng, J.; Ma, H. Structural and Optoelectronic Properties of Two-Dimensional Ruddlesden–Popper Hybrid Perovskite $CsSnBr_3$. *Nanomaterials* **2021**, *11*, 2119. [CrossRef] [PubMed]